Optimal Rule-of-Thumb Design of Nickel-Vanadium Oxides as Electrochromic Electrode with Ultrahigh Capacity and Ultrafast Color Tunability

Harish S. Chavan, [†] *Bo Hou,* [‡+] *Yongcheol Jo,* [†,§] *Akbar I. Inamdar,* *[†] *Hyunsik Im,* *[†] *Hyungsang Kim*[†]*

[†] Division of Physics and Semiconductor Science, Dongguk University, Seoul 04620, South Korea

[‡] Department of Engineering Science, University of Oxford, Parks Road, OX1 3PJ, UK

+ Present address: School of Physics and Astronomy, Cardiff University, Cardiff, CF24 3AA, Wales, UK.

[,§] Quantum-functional Research Centre, Dongguk University, Seoul 04620, South Korea

KEYWORDS: electrochromic supercapacitor; bimetallic NiV oxide; optical modulation; ultra-fast response.

ABSTRACT

The use of electrodes capable of functioning as both electrochromic windows and energy storage devices has been extended from green building development to various electronics and displays to promote more efficient energy consumption. Herein we report the electrochromic energy storage of bimetallic NiV oxide (NiVO) thin films fabricated using chemical bath deposition. The best optimized NiVO electrode with a Ni/V ratio of 3 exhibits superior electronic conductivity and a large electrochemical surface area, which are beneficial for enhancing electrochemical performance. The color switches between semi-transparent (a discharged state) and dark brown (a charged state) with excellent reproducibility due to the intercalation and deintercalation of OH^- ions in an alkaline KOH electrolyte. A specific capacity of 2403 Fg, a coloration efficiency of 63.18 cm^2C^{-1}, and an outstanding optical modulation of 68% are achieved. The NiVO electrode also demonstrates ultra-fast coloration and bleaching behavior (1.52 s and 4.79 s, respectively), which is considerably faster than the NiO electrode (9.03 s and 38.87 s). It retains 91.95% capacity after 2000 charge–discharge cycles, much higher than the NiO electrode (83.47%), indicating that it has significant potential for use in smart energy storage applications. The superior electrochemical performance of the best NiVO compound electrode with an optimum Ni/V compositional ratio is due to the synergetic effect between high electrochemically active surface area induced by V-doping improved redox kinetics (low charge-transfer resistance), and fast ion diffusion, which provides a facile charge transport pathway at the electrolyte/electrode interface.

Electrochromism is an interesting electrochemical phenomenon observed in oxides and conjugated polymers that have been actively employed in various fields, including energy-efficient smart windows, wearable devices, anti-glare rearview mirrors, military camouflage, Li ion batteries and displays.[1-5] This electrochemically reversible visualization technique can also be combined with various functional devices such as supercapacitors, smart windows, information displays, switchable mirrors, and dynamic shading elements.[6,7] Over the last two decades, supercapacitors have also received a considerable amount of interest as a promising energy storage technology due to their high capacitance, good cycling stability, and fast charge–discharge capabilities.[8-13]

Among various supercapacitor electrode materials, transition metal oxide (TMO)-based pseudocapacitors, which operate on the basis of reversible Faradaic reactions on the electrode surface, are known to have high power and energy densities and fast chargeability.[14-16] Recently, the fusion of energy storage and electrochromism technologies has created electrochromic supercapacitors (also known as smart supercapacitors) and has been employed in conjunction with energy storage, wearable technology, energy harvesting, thermal control, and sensing technology.[17-31] Various strategies have been employed in the design and compositional optimization of nanostructures to maximize their electrochemical performance by taking advantage of the synergetic effect between porous structures and a higher electrode conductivity. The nanostructure and porosity of TMO-based electrodes are beneficial for physiochemical characteristics such as ionic diffusivity and the electrochemically active surface area (ECSA), which strongly affect the dynamics of the surface reactions. The electrochemical reactions in TMO-based materials are associated with their multiple oxidation states, which favor intercalation reactions.[32]

WO_3, NiO and their complex hybrid materials are vastly studied for electrochromic supercapacitor applications due to their good electrochemical properties such as high coloration efficiency, high color contrast, high optical modulation and reversibility (Figure 1a and supplementary Table S1). However, they still suffer not only the absence of scalable, low-cost synthesis but also from the low specific capacitance values, poor cycle life, and long response time due to low electrical conductivity and slow diffusion kinetics. These drawbacks can be overcome by enhancing the reversible ionic diffusion reactions, increasing the number of electrochemically active sites, and improving electrochemical stability on the active surface. From a technical perspective, it is desirable to develop electrode materials with high electrical conductivity, a larger number of active states on a porous surface, and electrochemically and mechanically robust constituents. Because the morphological and electrochemical nature of TMO electrodes is strongly determined by the constituent metal elements, one practical approach for obtaining high-performance TMO-based electrodes is to optimize bimetallic TMOs by way of tuning the composition ratio of the metals involved. Environmentally benign NiO is one of the most suitable materials for this purpose because of its high coloration efficiency, high specific capacitance, outstanding cyclic reversibility, and good compatibility with other metals.

Herein we fabricate bimetallic $Ni_{1-x}V_xO$ ($0 \leq x \leq 1$) compounds via chemical bath deposition (CBD), tuning the composition ratio (x) systematically to maximize the electrochemical activity. Figure 1b shows a schematic of the CBD method and the evolution of the surface morphology of the $Ni_{1-x}V_xO$ films with increasing V content. Incorporating vanadium (V) into NiO enhances the chemical reaction due to its multiple oxidation states and plays a key role in determining surface morphologies. The best optimized bimetallic $Ni_{0.75}V_{0.25}O$ exhibits a high specific capacity of 2403 Fg^{-1} and a coloration efficiency of 63.18 $cm^2\,C^{-1}$, with a transition from semi-transparent to dark

brown and a higher optical modulation of 68%. More rapid coloration (1.52 s) and bleaching (4.79 s) is observed for the $Ni_{0.75}V_{0.25}O$ electrode compared with the pure NiO-based electrode. The best-performance $Ni_{0.75}V_{0.25}O$ electrode offers long-term cycling stability over 2000 colored/bleached (i.e., charge–discharge) cycles.

All of the chemicals were of analytical grade and used as received without further purification. Nickel chloride ($NiCl_2 \cdot 6H_2O$), sodium orthovanadate (Na_3VO_4), and ammonia solution were purchased from Sigma-Aldrich. All of the precursor solutions were freshly prepared using de-ionized (DI) water. Nanostructured bimetallic $Ni_{1-x}V_xO$ (NiVO) thin-film electrodes were synthesized on indium doped tin oxide (ITO) substrates using a CBD technique. Here, the chemical composition (x) corresponds to the Ni/V ratio in the precursor solution, and this precursor Ni/V ratio shows a similar tendency to the experimentally obtained Ni/V ratio. Prior to deposition, the ITO substrates were cleaned with acetone, methanol, and DI water. The precursor solutions were prepared by dissolving nickel chloride ($NiCl_2 \cdot 6H_2O$) and sodium orthovanadate (Na_3VO_4) in 60 ml of DI water. The molar ratio of Ni to V in the precursor solutions varied between 0.95:0.05 and 0.25:0.75. For comparison, pure NiO was also synthesized. The pH of the precursor solutions was adjusted to 13 by adding 10 ml of ammonia solution. This solution was then transferred to a glass beaker, into which the pre-cleaned ITO substrates were immersed vertically. The entire assembly was then heated at 80 °C for 10 h using a circulating water bath system. The solution was continuously stirred using a magnetic bar during the deposition process. After deposition, the films were rinsed with DI water and dried with N_2 gas. Subsequently, the films were annealed at 300 °C for 2 h to remove water and increase adhesion to the substrate.

X-ray diffraction (XRD) patterns for the films were recorded using an X-ray diffractometer with Ni-filtered Cu-Kα radiation (Ka α-1.54056 Å) (X'pert PRO, PANalytical). The surface

morphology was observed using field-emission scanning electron microscopy (FE-SEM; JSM-6701F, JEOL, Japan). The chemical state of the bimetallic NiVO films was investigated using X-ray photoelectron spectroscopy (XPS; ULVAC-PHI VersaProbe II), while their microscopic structural properties were investigated using transmission electron microscopy (JEOL 3000F) and high-angle annular dark-field (HAADF) scanning transmission electron microscopy (STEM) with an Oxford energy dispersive X-ray spectroscopy (EDAX) detector (JEM-2100). High-resolution transmission electron microscopy (HR-TEM) and selected area electron diffraction (SAED) were conducted at 300 kV. Optical transmittance was analyzed using a spectrophotometer. The mass of the active electrode was estimated using a standard weight difference method. A potentiostat (Princeton Applied Research, VersaSTAT 3) was used with a conventional three-electrode electrochemical cell containing a 2 M KOH electrolyte, $Ni_{1-x}V_xO$ as the working electrode, a saturated calomel electrode (SCE) as the reference electrode, and graphite as the counter-electrode. Electrochemical impedance spectroscopy (EIS) measurements were taken from 0.1 Hz to 10 kHz (AC) using an impedance analyzer.

Figure 2 shows the microstructural and structural properties of a $Ni_{0.75}V_{0.25}O$ thin-film electrode. Pure NiO exhibits a cauliflower-like morphology (Figure 2a and supplementary Figures S1a–d), while the $Ni_{0.75}V_{0.25}O$ electrode has a smooth silk-like morphology (Figure 2b and Figure 2c). With increasing V content in the NiVO film, the surface morphology changes dramatically (supplementary Figures S2–S7). The V-dependent morphology of the NiVO films is associated with complex growth reactions at different Ni/V ratios in the precursor solution. The growth mechanisms are determined by the pH, ionic conductivity, viscosity, and solute (i.e., salt) concentration of the solution. The V content in the precursor solution plays a crucial role in controlling the characteristic surface morphology of the NiVO film, which is presumably due to

the different values of the atomic radius of Ni (1.49 Å) and of V (1.71 Å). The lower atomic weight of V may promote the reaction rate, leading to a cauliflower-like morphology for NiO, a smooth silk-like morphology for $Ni_{0.75}V_{0.25}O$, and interconnected thin, porous flakes for $Ni_{0.25}V_{0.75}O$.

EDX measurements reveal that the real atomic molar ratios of Ni/V in the $Ni_{1-x}V_xO$ films are very similar to those of the precursor Ni/V solutions (supplementary Figures S2–S7). The SAED patterns of the $Ni_{0.75}V_{0.25}O$ (Figure 2d) exhibit ring patterns which indicate the polycrystalline nature of the electrode film.[33-35] Figure 2e presents the TEM image of the $Ni_{0.75}V_{0.25}O$ film, showing its thin, silk-like morphology. The HRTEM image in Figure 2f shows clear lattice fringes, with the lattice fringe spacing of 0.21 and 0.24 nm (Figure 2g and Figure 2h) corresponding to the (101) and (110) planes of NiO.[36] A continuous uniform distribution of the constituent elements is observed in the HAADF–STEM EDX mapping images for the $Ni_{0.75}V_{0.25}O$ sample (Figs. 2i–l). The STEM elemental line scan (supplementary Figures S8a,b) also reveals the uniform distribution of Ni, V, and O, even on a scale of a few micrometers.

Figure 3a presents the XRD patterns of the pure NiO and $Ni_{0.75}V_{0.25}$-O thin-film electrodes. The peaks indicated by the asterisk and the broad peak around 30° are associated with the ITO substrate. The diffraction peaks observed at 37.20°, 43.08°, and 62.76° correspond to the (111), (200), and (220) planes of the cubic structure of NiO (JCPDS 44-1159). There are no well-defined diffraction peaks in the measured XRD spectrum of $Ni_{0.75}V_{0.25}O$ due to the lattice distortion following V doping, resulting in the degradation of the crystalline quality.[33] The effect of V doping in NiO is confirmed by measuring the Raman spectra of the NiO and NiVO electrodes (Figure 3b). The broad peak at 497.13 cm^{-1} for the NiO sample was associated with the lattice vibrations of the Ni-O bonds.[37,38] The Raman spectrum for the $Ni_{0.75}V_{0.25}O$ sample differs dramatically. In particular, the peak intensity of the NiO vibrations tends to decrease slightly towards higher energies

(indicated by the dotted lines). The shift in the peak position provides clear evidence for the successful incorporation of V into the NiO. The Raman spectrum of the NiVO sample exhibits a peak centered at ~800 cm^{-1}, which is associated with the stretching modes of the $(VO_4)^{3-}$ tetrahedron. [39,40] The systematic evolution of the XRD patterns and the shift in the Raman peaks of the $Ni_{1-x}V_xO$ samples are presented in supplementary Figure S9.

Figure 3c shows the XPS survey spectrum of NiO and $Ni_{0.75}V_{0.25}O$, revealing the presence of Ni, V, and O in the bimetallic composite electrode. The XPS Ni 2*p* spectrum of NiO exhibits peaks at the binding energies of 854.8 eV and 872.4 eV, which correspond to the Ni^{2+} binding states of Ni $2p_{3/2}$ and Ni $2p_{1/2}$, respectively (Figure 3 d).[20, 41] The peaks located at 856.6 eV and 874.1 eV are due to the Ni^{3+} oxidation states,[33] while the other peaks are shakeup satellite peaks related to Ni^{2+} and Ni^{3+}. Interestingly, the binding states of Ni $2p_{3/2}$ and Ni $2p_{1/2}$ shift towards a high energy side by 0.8 eV relative to those of undoped NiO, suggesting the modification of the electronic structure upon V doping. This is because of the local chemical and physical environment of that Ni atom and the chemical nature of the neighboring atoms, such as the existence of atoms of higher oxidation states around it. Additionally, the reduced intensity of the satellite peaks at 856.6 eV and 874.1 eV upon V doping also indicates the formation of pure Ni^{2+} and Ni^{3+} states. Figure 3e shows the V $2p_{3/2}$ spectrum, which is deconvoluted into two peaks at 515.3 eV and 516.7 eV, and these are associated with the V^{3+} (V_2O_3) and V^{4+} (VO_2) oxidation states.[33] Finally, Figure 3f shows the O*1s* spectra of NiO and $Ni_{0.75}V_{0.25}O$. The V_2O_3 phase is clearly detected in the O 1*s* spectrum of the $Ni_{0.75}V_{0.25}O$ sample (528.9 eV). The deconvoluted peaks at 530.2 eV and 531.2 eV in the $Ni_{0.75}V_{0.25}O$ sample are associated with NiO and Ni_2O_3 respectively. The shift in the binding energy (~0.32 eV) in O 1*s* between NiO and $Ni_{0.75}V_{0.25}O$ is consistent with a similar shift observed in the Ni 2*p* spectra.

The electrochemical performance of the electrodes was investigated using a conventional three-electrode electrochemical cell in a 2M KOH electrolyte at room temperature. Figure 4a presents the cyclic voltammograms (CVs) for the NiO and $Ni_{0.75}V_{0.25}O$ electrodes recorded with a potential window of between –0.5 V to 0.9 V vs. SCE at a scan rate of 5 mV/s. The CV curves exhibit oxidation and reduction peaks (marked with arrows) during the anodic and cathodic scans, respectively, illustrating the pseudocapacitive nature of the electrodes.[8] During the anodic scan, both electrode films become dark brown due to oxidation before returning to their original transparent state during the cathodic scan due to the reduction of the electrode. These reversible oxidation and reduction processes are associated with the reversible transformation of Ni^{2+} to Ni^{3+} via the insertion and de-insertion of OH^- ions. The insertion of OH^- ions cause the electrode to become charged, while the de-insertion of OH^- ions discharge the electrode.

Figure 4b presents the chronocoulometry (CC) curves of the NiO and $Ni_{0.75}V_{0.25}O$ electrodes. The applied potential step was ± 1.2 V (vs. SCE) for a fixed time of 60 s. The constant positive/negative voltage allows the film to alternate between colored and bleached for 60 s each. The transmittance spectra of the colored and bleached films in a wavelength range of 300 to 800 nm are presented in Figure 4c. The difference in the transmittance is between the colored and bleached states at 630 nm: in other words, optical modulation is 68% for $Ni_{0.75}V_{0.25}O$, which is considerably larger than NiO (36%). This optical modulation analysis is consistent with the CC data, confirming that the electrochemical energy storage and electrochromism of the electrodes are associated with the same electrochemical mechanisms on the surface. The CV, CC, and transmittance spectra of the other $Ni_{1-x}V_xO$ samples are presented in the Supplementary Information (supplementary Figures S10–S14). The change in the optical density (ΔOD) and

coloration efficiency (CE) of the $Ni_{1-x}V_xO$ and NiO electrodes is estimated using the following equations:

$$(\Delta OD)_{630nm} = log\ (T_b / T_c) \quad (1)$$

$$CE_{630nm} = (\Delta OD) / (Q/A) \quad (2)$$

where T_b and T_c are the transmittance in the bleached and colored states, respectively, and Q/A is the charge density per unit area. The total charge density (Q/A) during the coloring and bleaching processes is estimated from the CC curves. The estimated electrochemical parameters for $Ni_{1-x}V_xO$ are provided in supplementary Table S2. The CE of the $Ni_{0.75}V_{0.25}O$ electrode is 63.18 cm^2C^{-1}, which is considerably higher than that of the other samples (16.95 cm^2C^{-1} for NiO).

The switching time is an important parameter used to evaluate the performance of an electrochromic supercapacitor and acts as an indicator of the kinetics during the electrochemical process. It is defined as the time required for a system to reach its fully colored and bleached states under alternating potentials. Figure 4d presents the chronoamperometric (CA) curves for the $Ni_{0.75}V_{0.25}O$ and NiO samples recorded with potential steps of ± 1.2 V (vs. SCE) for a fixed time of 60 s over 5 cycles. The switching time for the $Ni_{0.75}V_{0.25}O$ electrode for coloration and bleaching is found to be 1.52 s and 4.79 s, respectively, which is significantly faster than those of the pure NiO electrode (9.03 s for coloring and 38.87 s for bleaching). The estimated switching times for the full range of $Ni_{1-x}V_xO$ electrodes are presented in the Supplementary Information (Figure S15).

The fast-switching time of an electrochromic material or device is mainly determined by the following factors: *i*) the electronic conductivity of the electrode, *ii*) the electrochemically active surface area (ECSA), *iii*) ionic diffusion within the electrochromic material, *iv*) ionic conductivity, *v*) film thickness, and *vi*) the composition/concentration of the electrolyte.[42,43] The ionic conductivity, film thickness, and composition/concentration of the electrolyte are not taken into

consideration because they are assumed to be similar for all of the samples. The observed superior switching time of the NiVO electrode was associated with its improved redox kinetics, which is directly related to electron transport within the electrochromic film (i.e., the electronic conductivity of the electrochromic electrode). EIS analysis of all the samples reveals that the $Ni_{0.75}V_{0.25}O$ sample has a lower charge transfer resistance of 12.53 Ω than the other samples (15.09 - 479.2 Ω). Detailed analysis of the EIS results is provided in the Supplementary Information (supplementary Figure S16 and Table S3).

We also evaluate the electrochemically active surface area (ECSA) of all the samples by measuring their CV curves at different scan rates (supplementary Figure S17 and Figure S18). The $Ni_{0.75}V_{0.25}O$ sample has a higher ECSA (2092 cm^2) than the other samples (56-934 cm^2). Finally, we estimate the diffusion coefficients for all the samples using the measured CVs (supplementary Figure S19) and the Randles-Servick equation.[44,45] The details for the diffusion coefficient calculations are provided in the Supplementary Information. The estimated diffusion coefficient (13.05×10^{-10} cm^2s^{-1}) of the $Ni_{0.75}V_{0.25}O$ sample is considerably higher than those ($2.61 - 9.49 \times 10^{-10}$ cm^2s^{-1}) of the other samples (see supplementary Table S4). Thus, based on the above analysis, it is reasonable to conclude that the faster switching time of the $Ni_{0.75}V_{0.25}O$ electrode is associated with its high conductivity and high diffusion coefficient, which provide efficient paths for electrons and a larger contact area at the electrolyte/electrode interface. Figure 4e presents the photographs of the $Ni_{0.75}V_{0.25}O$ sample taken in its colored and bleached states. The semi-transparent as-grown NiV film becomes dark brown following coloration at +1.2 V (vs. SCE, fully charged state) for 60 s, and it returns to its original state at the opposite potential of −1.2 V (vs. SCE, fully discharged state). The as-grown and bleached samples show no difference in transparency and uniformity, suggesting that the electrode has good reversibility and sensitivity.

The electrochemical energy storage properties of the $Ni_{1-x}V_xO$ and NiO electrodes were also tested. Figures 5a and b display the measured galvanostatic charge–discharge (GCD) profiles of the NiO and $Ni_{0.75}V_{0.25}O$ electrodes, respectively, measured at various current densities. Images of the $Ni_{0.75}V_{0.25}O$ electrode in the as-grown, charged, and discharged states are shown in Figure 5c. The stored energy level of the electrode between the charged (dark brown) and uncharged (semi-transparent) states was monitored by its color. The GCD curves of the other $Ni_{1-x}V_xO$ samples are presented in the Supplementary Information (Figure S20). The time required to charge and discharge the electrodes is measured for a potential window of 0 to 0.42 V (vs. SCE). The non-linear nature of the GCD curves confirms the pseudocapacitive behavior of the electrodes.[19-21] The discharge curves exhibit two slopes: IR drop and capacitive component. The specific capacity of the electrodes is calculated using Eq. (3):

$$Cs = I\Delta t/m\Delta V \qquad (3)$$

where I and m represent the discharge current and the mass of the active material, respectively. ΔV and Δt are the potential window and total discharge time, respectively. Figure 5d shows the specific capacity of the NiO and $Ni_{0.75}V_{0.25}O$ electrodes at different current densities for 5 cycles. The specific capacity values of the other samples are presented in supplementary Figure S21a and Table S5. The specific capacity decreases gradually with an increasing current density. The average specific capacity of the $Ni_{0.75}V_{0.25}O$ electrode is found to be 2403 Fg^{-1} at a current density of 1 Ag^{-1}, which is much larger than that of NiO (1333 Fg^{-1}). This value is also superior to those obtained from other electrochromic supercapacitive materials reported in the literature (Figure 1 and supplementary Table S6).[46-49] Figure 5e and supplementary Figure S21b show the Ragone plots of the $Ni_{1-x}V_xO$ samples. The $Ni_{0.75}V_{0.25}O$ electrode exhibits a higher energy density than the other samples, which is in agreement with the other results.

The long-term electrochemical stability of the electrodes was evaluated using GCD measurements at a current density of 5 Ag^{-1} for 2000 cycles. Figure 5f shows the long-term cycling stability of the NiO and $Ni_{0.75}V_{0.25}O$ electrodes. The initial specific capacity of the NiO and $Ni_{0.75}V_{0.25}O$ electrodes is 357 Fg^{-1} and 956 Fg^{-1}, respectively. The capacity retention of the NiO and $Ni_{0.75}V_{0.25}O$ electrodes after 2000 charge–discharge cycles is 83.47% and 91.95%, respectively.

To understand the electrochemical reaction mechanism of the best-performing $Ni_{0.75}V_{0.25}O$ electrode, we carried out ex-situ XPS measurements for the colored (i.e., charged) and bleached (i.e., discharged) states. Figure 6a presents the XPS survey spectra of the $Ni_{0.75}V_{0.25}O$ sample in the colored or bleached states. The XPS spectra display the core-level peaks for Ni, V, O, and C. The presence of the 0KLL peak in the bleached and colored states is associated with the KOH electrolyte. The peak intensity of the Ni $2p_{3/2}$ signal is significantly higher in the colored state than in the bleached state, indicating the introduction of OH^- ions to the surface of the electrode. The Ni $2p_{3/2}$ core-level spectrum in the colored state exhibits two peaks at 855.5 eV and 861.5 eV (Figure 6b), which correspond to Ni^{3+} oxidation states. The Ni $2p_{3/2}$ core-level spectrum in the bleached state exhibits peaks at 854.79 eV and 860.46 eV, which correspond to Ni^{2+} oxidation states. The peak positions in the colored state shift to higher values by 0.71 eV and 1.06 eV in the bleached state due to the conversion of Ni^{2+} to Ni^{3+}. Thus, it is evident that OH^- ion intercalation causes the coloration of the $Ni_{0.75}V_{0.25}O$ film. Similarly, V in the film undergoes a transition from V^{3+} (515.7 eV in the bleached state) to V^{4+} (516.4 eV in the colored state), as shown in Figure 6c. The corresponding O 1*s* spectra are shown in Figure 6d. The O 1*s* spectrum in the bleached state can be deconvoluted into three broad peaks at 529.2 eV, 530.6 eV and 532.4 eV which correspond to V_2O_3, NiO and Ni_2O_3, respectively. On the other hand, the relative magnitude of these phases

in the colored state changes due to the incorporation of OH^- ions and oxidation of Ni and V. The increased intensity of the NiO and V_2O_3 phases clearly suggest the oxidation of the electrode during the coloration process.

In summary we have demonstrated the CBD synthesis and electrochemical properties of bimetallic NiVO compound films as high-performance electrodes for electrochromic supercapacitor applications. The NiVO compound electrode is optimized by tuning the composition ratio of Ni and V. The optimal Ni/V ratio enhances the electronic conductivity and ECSA of the NiVO compound electrode. The optimized NiVO electrode demonstrates excellent electrochemical energy storage and electrochromic properties, with a specific capacity of 2403 Fg^{-1} at 1A/g (932 Fg^{-1} at 5 A/g) and a coloration efficiency of 63.18 $cm^2\,C^{-1}$ at a wavelength of 630 nm, both of which are clearly superior to those obtained from other metal oxide-based electrochromic supercapacitor materials. The optimized NiVO electrode switches between the colored (dark-brown) and bleached (semi-transparent) states with an optical modulation of 68% and with ultra-fast switching times of 1.52 s (coloration) and 4.79 s (bleaching). The enhanced specific capacitance and switching time of the optimized NiVO film with an optimum Ni/V ratio are associated with a high electrochemically active surface area induced by V-doping, improved redox kinetics (low charge-transfer resistance), and fast ion diffusion, all of which facilitate the rapid charge transport between the electrolyte/electrode interface.

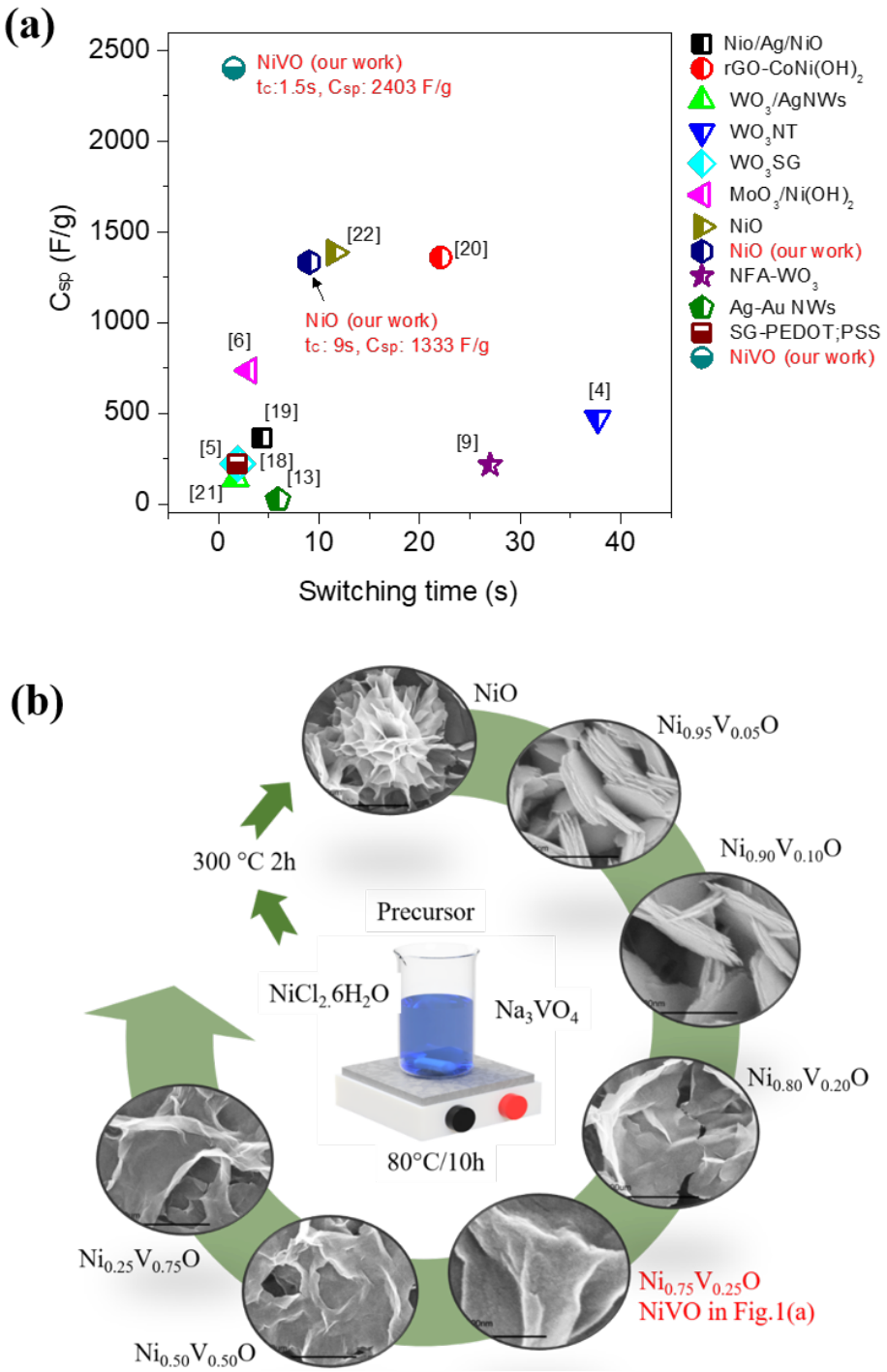

Figure 1. Literature survey results and comparison of specific capacitance (Csp:F/g) and switching time (s) for various transition metal oxide (TMO) based electrochromic supercapacitor electrodes, including our samples. (b) Schematic showing the growth processes of the Ni_xV_{1-x} oxides using chemical bath deposition (CBD), along with their morphologies. As discussed in the main text, the best-performance sample is $Ni_{0.75}V_{0.25}O$.

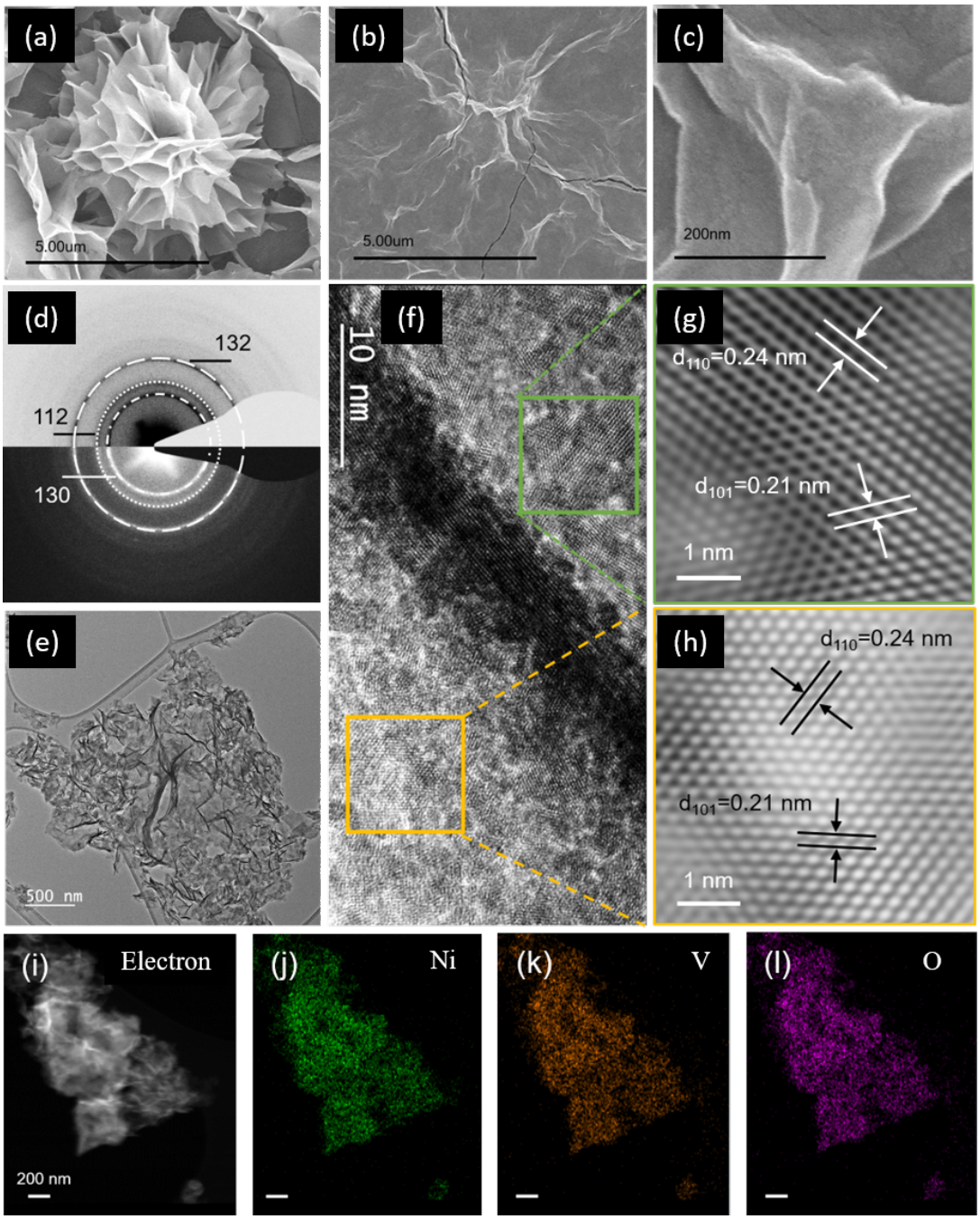

Figure 2. Structural and microstructural analysis. SEM images of the (a) pure NiO and (b, c) $Ni_{0.75}V_{0.25}O$ at different magnifications. (d) Selected area electron diffraction (SAED) pattern exhibiting diffused ring patterns. (e) TEM, (f) HRTEM, and (g, h) an enlarged selected-area HRTEM image which show clear lattice fringes with a distance of 21 and 24 nm, respectively. (i–l) HAADF-STEM EDX elemental mapping, reveal the homogeneous distributions of Ni (green), V (orange), and O (pink) in the sample.

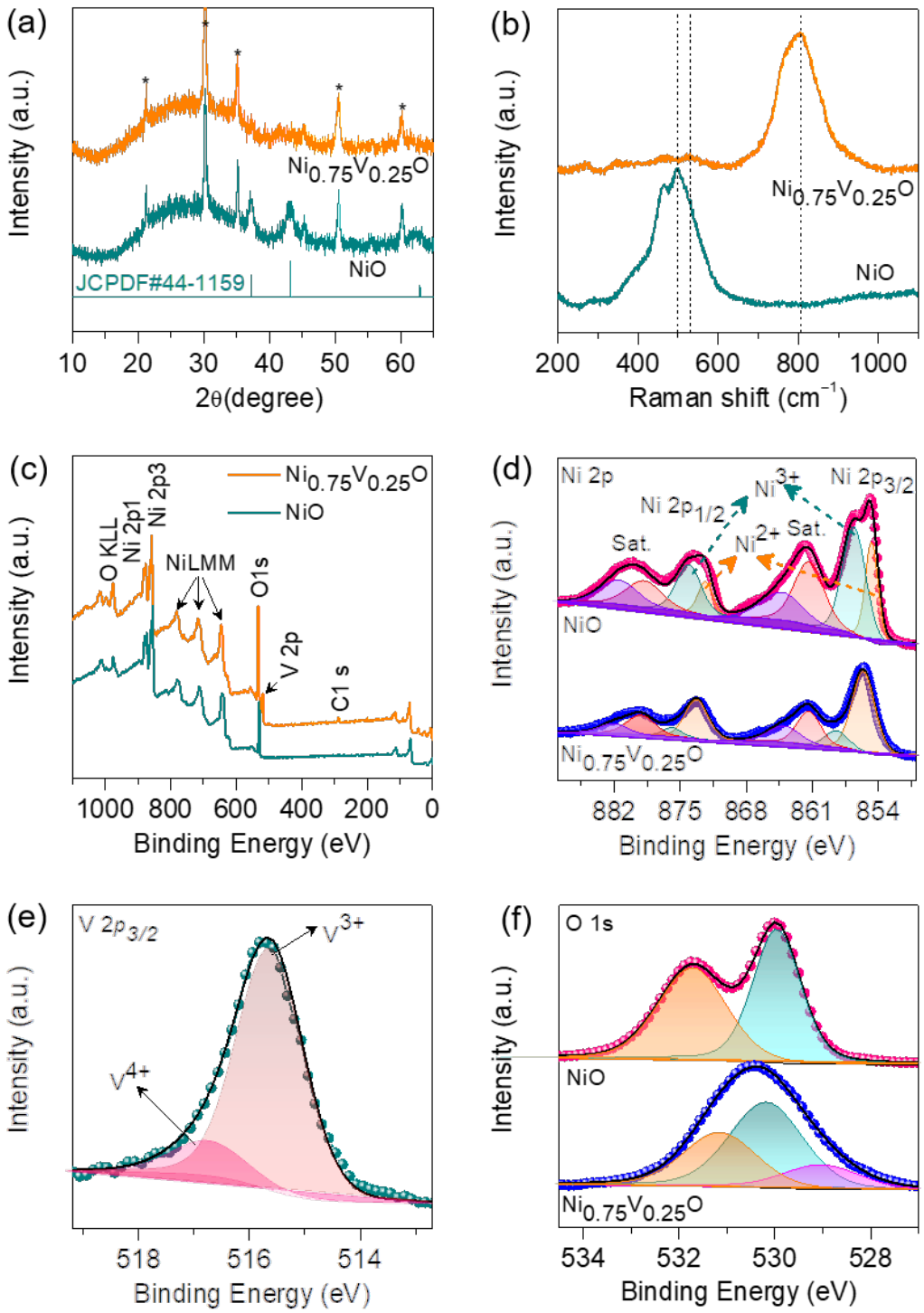

Figure 3. (a) X-ray diffraction patterns of NiO and $Ni_{0.75}V_{0.25}O$ together with JCPDS standards (44-1159). (b) Raman spectra of NiO and $Ni_{0.75}V_{0.25}O$. XPS analysis of $Ni_{0.75}V_{0.25}O$: (c) survey spectra showing the presence of Ni, V, and O, (d) core level Ni *2p*, (e) core level V $2p_{3/2}$, and (f) O *1s*.

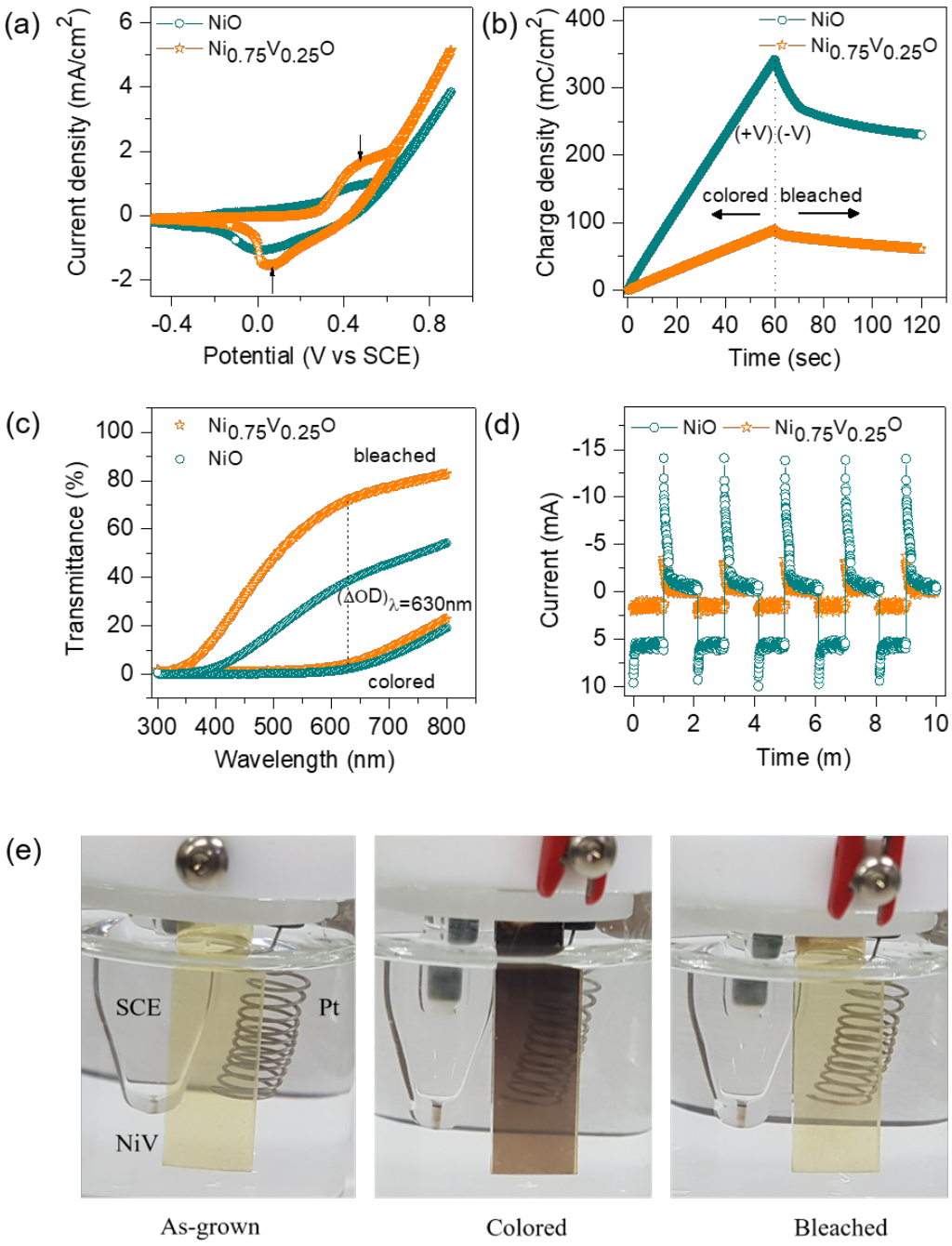

Figure 4. (a) Cyclic voltammogram of NiO and $Ni_{0.75}V_{0.25}O$ recorded in a 2M KOH electrolyte at a scan rate of 5mV/s. (b) Chronocoulometry measurements for the colored film at ± 0.6 V. (c) Optical transmittance spectra for NiO and $Ni_{0.75}V_{0.25}O$ in a colored and bleached state. (d) Chronoamperometric curves for the $Ni_{0.75}V_{0.25}O$ and NiO samples recorded with a potential step of ± 1.2 V (vs. the SCE) for a fixed time of 60 s. (e) Images of $Ni_{0.75}V_{0.25}O$ samples taken in a colored and bleached state.

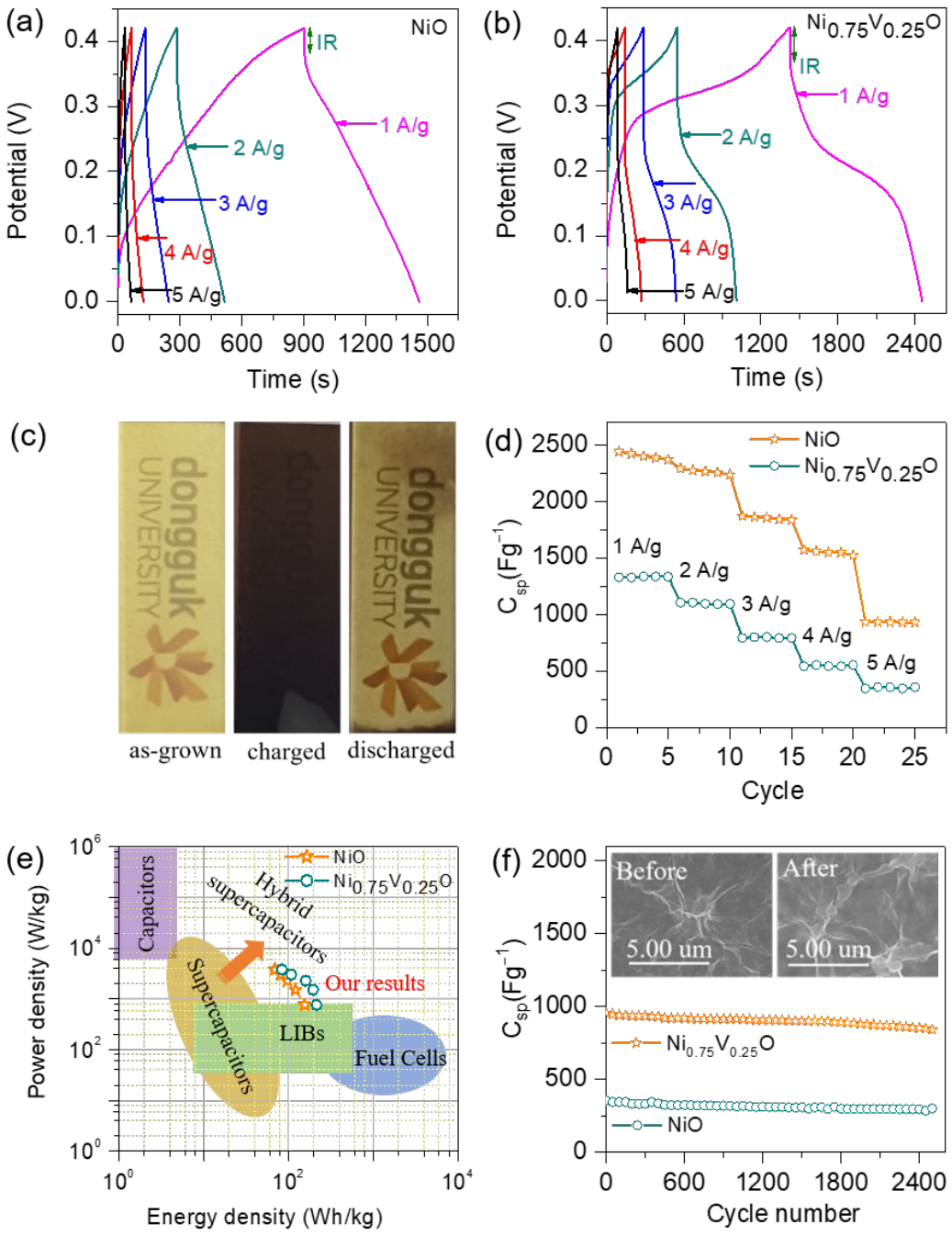

Figure 5. Galvanostatic charge–discharge (GCD) curves for (a) NiO and (b) $Ni_{0.75}V_{0.25}O$ recorded at different current densities. (c) Images of $Ni_{0.75}V_{0.25}O$ samples taken in a charged and discharged state. (d) Specific capacitance obtained from the GCD curves at various current densities. (e) calculated energy density and power density (Ragone plot). (f) Cycling stability test at a high current density of 5 Ag^{-1} for over 5000 charge–discharge cycles.

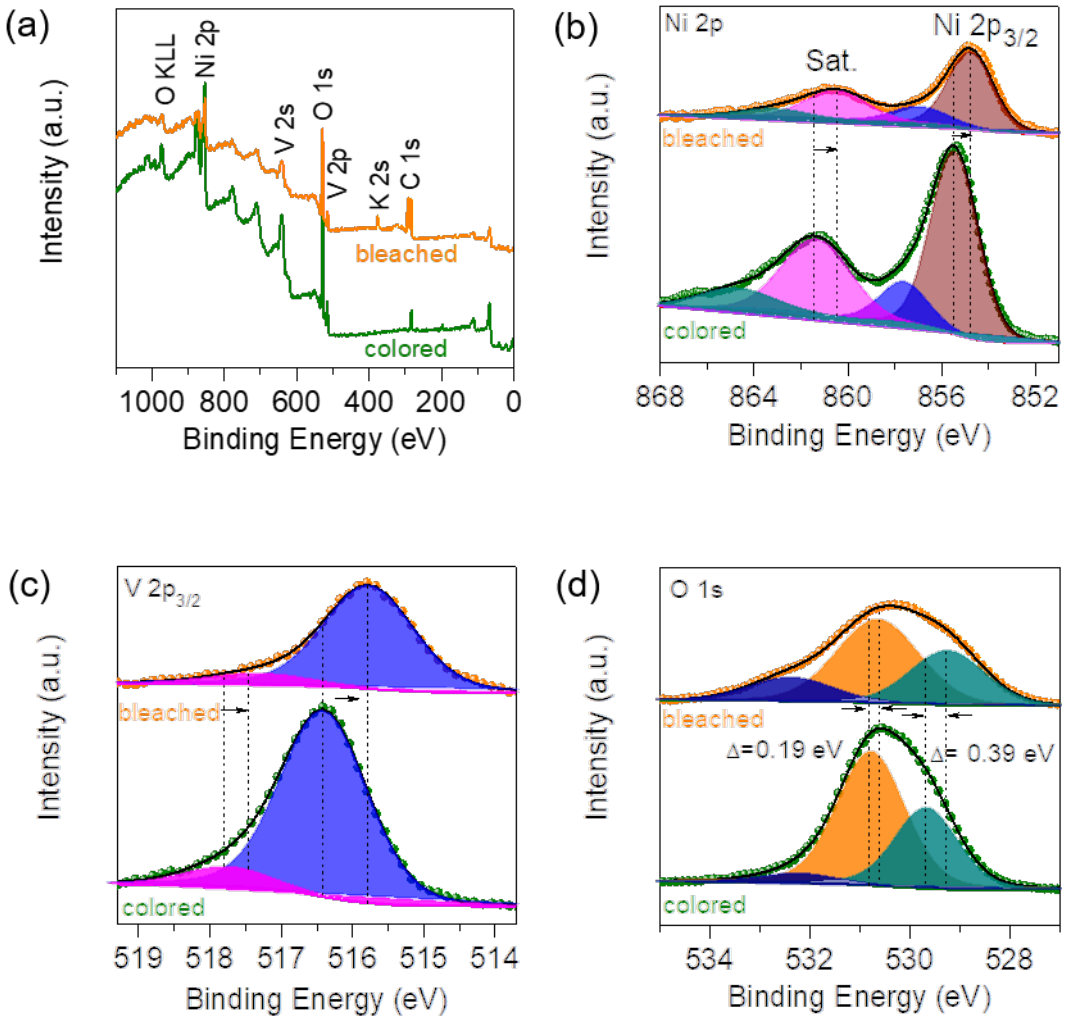

Figure 6. Ex-situ XPS analysis of $Ni_{0.75}V_{0.25}O$ in a colored and bleached state: (a) survey spectra, (b) core-level Ni $2p_{3/2}$ revealing a shift towards higher energy after coloration, (c) core-level V $2p_{3/2}$ showing the oxidation of the electrode during the coloration process, and (d) core-level O *1s*.

ASSOCIATED CONTENT

Supporting Information

The Supporting Information is available free of charge via the Internet at http://pubs.acs.org. Additional Literature survey, characterization data such as SEM images, XRD patterns, HAADF-STEM image, Raman spectra, electrochemical measurements, transmittance spectra, electrochemical impedance spectroscopy measurements, and galvanostatic charge–discharge curves are included.

AUTHOR INFORMATION

***Corresponding Authors**

*E–mail: akbarphysics2002@gmail.com (A. I. I.)

*E–mail: hyunsik7@dongguk.edu (H. I.)

*E–mail: hskim@dongguk.edu (H. K.)

Authors Contributions

H.S.C, A.I.I., H.K., and H. I. designed the experiments and wrote the manuscript. H.S.C. carried out the experiments and extracted data for the analysis. B.H. carried out electron microscopy, Y.J helps for the data analysis. All of the authors have reviewed and approved the final version of the manuscript.

Acknowledgments

This work was supported by the Basic Science Research Program of the National Research Foundation of Korea (2018R1D1A1B07049046, 2021R1A2B5B01001796 and 2021R1A4A5031805).

Conflict of Interest

The authors declare no conflict of interest

References

(1) Chen, J.; Wang, Z.; Chen, Z.; Cong, S.; Zhao, Z. Fabry−Perot Cavity-Type Electrochromic Supercapacitors with Exceptionally Versatile Color Tunability. *Nano Lett.* **2020**, *20*, 1915−1922.

(2) Tian, Y.; Su, Y.; Chen, H.; Li, Q.; Geng, F.; Cong, S.; Zhao, Z. Synergy of $W_{18}O_{49}$ and Polyaniline for Smart Supercapacitor Electrode Integrated with Energy Level Indicating Functionality. *Nano Lett.* **2014**, *14*, 2150−2156.

(3) Inamdar, A. I.; Kim, Y. S.; Jang, B. U.; Im, H.; Jung, W.; Kim, D.Y.; Kim, H. Effects of oxygen stoichiometry on electrochromic properties in amorphous tungsten oxide films. *Thin Solid Films* **2012**, *520*, 5367–5371.

(4) Kim, J.; Ong, G. K.; Wang, Y.; LeBlanc, G.; Williams, T. E.; Mattox, T. M.; Helms, B. A.; Milliron, D. J. Nanocomposite Architecture for Rapid, Spectrally-Selective Electrochromic Modulation of Solar Transmittance. *Nano Lett.* **2015**, *15,* 5574−5579.

(5) Kalagi, S. S.; Mali, S. S.; Dalavi, D. S.; Inamdar, A. I.; Im, H.; Patil, P. S. Limitations of dual and complementary inorganic–organic electrochromic device for smart window application and its colorimetric analysis. *Synthetic Metals* **2011**, *161*, 1105–1112.

(6) Liang, H.; Li, R.; Li, C.; Hou, C.; Li, Y.; Zhang, Q.; Wang, H. Regulation of carbon content in MOF-derived hierarchical-porous NiO@C films for high-performance electrochromism. *Mater. Horiz*. **2019**, *6*, 571–579.

(7) Wen, R. T.; Granqvist, C. G.; Niklasson, G. A. Eliminating degradation and uncovering ion-trapping dynamics in electrochromic WO_3 thin films. *Nat. Mater*. **2015**, *14*, 996–1001.

(8) Inamdar, A. I.; Kim, Y. S.; Pawar, S. M.; Kim, J. H.; Im, H.; Kim, H. Chemically grown, porous, nickel oxide thin-film for electrochemical supercapacitors. *J. Power Sources* **2011**, *196*, 2393–2397.

(9) Kim, J.; Ju, H.; Inamdar, A. I. Jo, Y.; Han, J.; Kim, H.; Im, H. Synthesis and enhanced electrochemical supercapacitor properties of Ag–MnO_2–polyaniline nanocomposite electrodes. *Energy* **2014**, *70*, 473–477.

(10) Inamdar, A.I.; Jo, Y.; Kim, J.; Han, J.; Pawar, S. M.; Kalubarme, R.S.; Park, C. J.; Hong, J. P.; Park, Y. S.; Jung, W.; Kim, H.; Im, H. Synthesis and enhanced electrochemical supercapacitive properties of manganese oxide nanoflake electrodes. *Energy* **2015**, *83*, 532–538.

(11) Cho, S.; Lee, S.; Hou, B.; Kim, J.; Jo, Y.; Woo, H.; Pawar, S. M.; Inamdar, A. I.; Park, Y.; Cha, S.; Kim, H.; Im, H. Optimizing nanosheet nickel cobalt oxide as an anode material for bifunctional electrochemical energy storage and oxygen electrocatalysis. *Electrochim. Acta* **2018**, *274*, 279–287.

(12) Sun, J. Q.; Li, W. Y.; Zhang, B. J.; Li, G.; Jiang, L.; Chen, Z. G.; Zou, R. J.; Hu, J. Q. 3D core/shell hierarchies of MnOOH ultrathin nanosheets grown on NiO nanosheet arrays for high-performance supercapacitors. *Nano Energy* **2014**, *4*, 56–64.

(13) Chavan, H. S.; Hou, B.; Ahmed, A. T. A.; Kim, J.; Jo, Y.; Cho, S.; Park, Y.; Pawar, S. M.; Inamdar, A. I.; Cha, S.; Kim, H.; Im, H. Ultrathin Ni-Mo oxide nanoflakes for high-performance supercapacitor electrodes. *J. Alloys Compd*. **2018**, *767*, 782–788.

(14) Pawar, S. M.; Pawar, B. S.; Babar, P. T.; Ahmed, A. T. A.; Chavan, H. S.; Jo, Y.; Cho, S.; Kim, J.; Hou, B.; Inamdar, A. I.; Cha, S.; Kim, J. H.; Kim, T. G.; Kim, H.; Im, H. Nanoporous

$CuCo_2O_4$ nanosheets as a highly efficient bifunctional electrode for supercapacitors and water oxidation catalysis. *Appl. Surf. Sci*. **2019**, *470*, 360–367.

(15) Lalwani, S.; Munjal, M.; Singh, G.; Sharma, R. K. Layered nanoblades of iron cobaltite for high performance asymmetric supercapacitors. *Appl. Surf. Sci*. **2019**, *476*, 1025–1034.

(16) Huang, H.; Zhang, H.; Fan, Y.; Deng, X.; Lia, G.; Liang, X.; Zhou, W.; Guo, J.; Tang, S. Serrated-like $NiCoO_2$ nanoarrays on Ni foam for high-performance supercapacitors. *Appl. Surf. Sci*. **2019**, *481*, 1220–1227.

(17) Scherer, M. R. J.; Steiner, U. Efficient Electrochromic Devices Made from 3D Nanotubular Gyroid Networks. *Nano Lett*. **2013**, *13*, 3005−3010.

(18) Chen, Z.; Peng, Y.; Liu, F.; Le, Z.; Zhu, J.; Shen, G.; Zhang, D.; Xiao, S.; Liu, C. P.; Lu, Y.; Li, H. Hierarchical Nanostructured WO_3 with Biomimetic Proton Channels and Mixed Ionic-Electronic Conductivity for Electrochemical Energy Storage. *Nano Lett.* **2015**, *15*, 802−6808.

(19) Inamdar, A. I.; Kim, J.; Jo, Y.; Woo, H.; Cho, S.; Pawar, S. M.; Lee, S.; Gunjakar, J. L.; Cho, Y.; Hou, B.; Cha, S.; Kwak, J.; Park, Y.; Kim, H.; Im, H. Highly efficient electro-optically tunable smart-supercapacitors using an oxygen-excess nanograin tungsten oxide thin film. *Sol. Energy Mater. Sol. Cells* **2017**, *166*, 78–85.

(20) Chavan, H. S.; Hou, B.; Ahmed, A. T. A.; Jo, Y.; Cho, S.; Kim, J.; Pawar, S. M.; Cha, S.; Inamdar, A. I.; Im, H.; Kim, H. Nanoflake $NiMoO_4$ based smart supercapacitor for intelligent power balance monitoring. *Sol. Energy Mater. Sol. Cells* **2018**, *185*, 166–173.

(21) Inamdar, A. I.; Chavan, H. S.; Kim, H.; Im, H. Mesoporous Ni-PANI composite electrode for electrochromic energy storage applications. *Sol. Energy Mater. Sol. Cells* **2019**, *201*, 110121.

(22) Yang, P.; Sun, P.; Mai, W. Electrochromic energy storage devices. *Mater. Today* **2016**, *19*, 394–402.

(23) Shen, L.; Du, L.; Tan, S.; Zang, Z.; Zhao, C.; Mai, W. Flexible electrochromic supercapacitor hybrid electrodes based on tungsten oxide films and silver nanowires. *Chem. Comm*. **2016**, *52*, 6296–6299.

(24) Cai, G.; Darmawan, P.; Cui, M.; Wang, J.; Chen, J.; Magdassi, S.; Lee, P. S. Highly Stable Transparent Conductive Silver Grid/PEDOT:PSS Electrodes for Integrated Bifunctional Flexible Electrochromic Supercapacitors. *Adv. Energy Mater*. **2016**, *6*, 1501882.

(25) Cai, G.; Wang, X.; Cui, M.; Darmawan, P.; Wang, J.; Eh, A. L.-S.; Lee, P. S. Electrochromo-supercapacitor based on direct growth of NiO nanoparticles. *Nano Energy*

2015, *12*, 258–267.

(26) Kim, J.; Inamdar, A. I.; Jo, Y.; Cho, S. Ahmed, A.T. A.; Hou, B.; Cha, S.; Kim, T.; Kim, H.; Im, H. Nanofilament array embedded tungsten oxide for highly efficient electrochromic supercapacitor electrodes. *J. Mater. Chem. A* **2020**, *8*, 13459–13469.

(27) Bi, Z.; Li, X.; Chen, Y.; He, X.; Xu, X.; Gao, X. Large-Scale Multifunctional Electrochromic-Energy Storage Device Based on Tungsten Trioxide Monohydrate Nanosheets and Prussian White. *ACS Appl. Mater. Interfaces* **2017**, *9*, 29872–29880.

(28) Zhong, Y.; Chai, Z.; Liang, Z.; Sun, P.; Xie, W.; Zhao, C.; Mai, W. Electrochromic Asymmetric Supercapacitor Windows Enable Direct Determination of Energy Status by the Naked Eye. *ACS Appl. Mater. Interfaces* **2017**, *9*, 34085–34092.

(29) Yun, T. G.; Park, M.; Kim, D. H.; Kim, D.; Cheong, J. Y.; Bae, J. G.; Han, S. M.; Kim, I. D.; All-Transparent Stretchable Electrochromic Supercapacitor Wearable Patch Device. *ACS Nano* **2019**, *13*, 3141–3150.

(30) Heo, S.; Dahlman, C. J.; Staller, C. M.; Jiang, T.; Dolocan, A.; Korgel, B. A.; Milliron, D. J. Enhanced Coloration Efficiency of Electrochromic Tungsten Oxide Nanorods by Site Selective Occupation of Sodium Ions. *Nano Lett*. **2020**, *20*, 2072–2079.

(31) Chen, Y.; Wang, Y.; Sun, P.; Yang, P.; Du, L.; Mai, W. Nickel oxide nanoflake-based bifunctional glass electrodes with superior cyclic stability for energy storage and electrochromic applications. *J. Mater. Chem. A* **2015**, *3*, 20614–20618.

(32) Zhu, L.; Peh, C. K. N.; Zhu, T.; Lim, Y. F.; Ho, G. W. Bifunctional 2D-on-2D MoO_3 nanobelt $Ni(OH)_2$ nanosheets for supercapacitor-driven electrochromic energy storage. *J. Mater. Chem. A* **2017**, *5*, 8343–8351.

(33) Wu, Z.; Khalafallah, D.; Teng, C.; Wang, X.; Zou, Q.; Chen, J.; Zhi, M.; Hong, Z. Vanadium doped hierarchical porous nickel-cobalt layered double hydroxides nanosheet arrays for high-performance supercapacitor. *J. Alloys Compd*. **2020**, *838*, 155604.

(34) Hou, B.; Parker, D.; Kissling, G. P.; Jones, J. A.; Cherns, D.; Fermín, D. J. Structure and Band Edge Energy of Highly Luminescent $CdSe_{1-x}Te_x$ Alloyed Quantum Dots. *J. Phys. Chem. C* **2013**, *117*, 6814–6820.

(35) Kudilatt, H.; Hou, B.; Welland, M. E. Quantum Dots Microstructural Metrology: From TimeResolved Spectroscopy to Spatially Resolved Electron Microscopy. *Part. Part. Syst. Charact*. **2020**, *37*, 2000192.

(36) Liu, D.; Li, D.; Yang, D. Size-dependent magnetic properties of branchlike nickel oxide nanocrystals. *AIP Advances* **2017**, *7*, 015028.

(37) Ahmed, A. A.; Hashim, M. R.; Rashid, M. Control of the structural, electrical and optical properties of spin coated NiO films by varying precursor molarity. *Thin Solid Films* **2019**, *690*, 137554.

(38) Dao, V. D.; Larina, L. L.; Jung, K. D.; Leed, J. K.; Choi, H. S. Graphene–NiO nanohybrid prepared by dry plasma reduction as a low-cost counter electrode material for dye-sensitized solar cells. *Nanoscale* **2014**, *6*, 477–482.

(39) Kellerman, D. G.; Chukalkin, T. G.; Medvedeva, N. I.; Kuznetsov, M. V.; Mukhina, N. A.; Semenova, A. S.; Gorshkov, V. S. Hydrogen reduction of vanadium in vanadium-doped $LiMnPO_4$. *Mater. Chem. and physics* **2015**, *149–150*, 209–215.

(40) Baddour-Hadjean, R.; Smirnov, M. B.; Smirnov, K. S.; Kazimirov, V. Y.; Gallardo-Amores, J. M.; Amador, U.; Arroyo-de Dompablo, M. E.; Pereira-Ramos, Lattice Dynamics of β-V_2O_5: Raman Spectroscopic Insight into the Atomistic Structure of a High-Pressure Vanadium Pentoxide Polymorph. J. P. *Inorg. Chem*. **2021**, 51, 3194–3201.

(41) Inamdar, A. I.; Kalubarme, R. S.; Kim, J.; Jo, Y.; Woo, H.; Cho, S.; Pawar, S. M.; Park, C. J.; Lee, Y. W.; Sohn, J. I.; Cha, S.; Kwak, J.; Kim, H.; Im, H. Nickel titanate lithium-ion battery anodes with high reversible capacity and high-rate long-cycle life performance. *J. Mater. Chem. A* **2016**, *4*, 4591–4699.

(42) Xu, T.; Walter. E. C.; Agrawal, A.; Bohn, C.; Velmurugan, J.; Zhu, W.; Lezec, H. J.; Talin, A. A. High-contrast and fast electrochromic switching enabled by plasmonics. *Nat. Commun*. **2016**, *7*, 10479.

(43) Chun, Y. T.; Neeves, M.; Smithwick, Q.; Placido, F.; Chu, D. High optical and switching performance electrochromic devices based on a zinc oxide nanowire with poly(methyl methacrylate) gel electrolytes. *Appl. Phys. Lett*. **2014**, *105*, 193301.

(44) Su, C.; Qiu, M.; An, Y.; Sun, S.; Zhao, C.; Mai, W. Controllable fabrication of α-$Ni(OH)_2$ thin films with preheating treatment for long-term stable electrochromic and energy storage applications. *J. Mater. Chem. C* **2020**, *8*, 3010–3016.

(45) Chen, P.-W.; Chang, C.-T.; Ko, T.-F.; Hsu, S.-C.; Li, K.-D.; Wu, J.-Y. Fast response of complementary electrochromic device based on WO_3/NiO electrodes. *Sci. Rep*. **2020**, *10*, 8430.

(46) Wei, D.; Scherer, M. R. J.; Bower, C.; Andrew, P.; Ryhanen, T.; Steiner, U. A Nanostructured Electrochromic Supercapacitor. *Nano Lett*. **2012**, *12*, 1857–1862.

(47) Wang, Y. H.; Wang, C. C.; Cheng, W. Y.; Lu, S. Y. Dispersing WO_3 in carbon aerogel makes an outstanding supercapacitor electrode material. *Carbon* **2014**, *69*, 287–293.

(48) Grote, F.; Yu, Z. Y.; Wang, J. L.; Yu, S. H.; Lei, Y. Self-Stacked Reduced Graphene Oxide Nanosheets Coated with Cobalt–Nickel Hydroxide by One-Step Electrochemical Deposition toward Flexible Electrochromic Supercapacitors. *Small* **2015**, *11*, 4666–4672.

(49) Dong, W.; Lv, Y.; Zhang, N.; Xiao, L.; Fan, Y.; Liu, X. Trifunctional NiO–Ag–NiO electrodes for ITO-free electrochromic supercapacitors. *J. Mater. Chem. C* **2017**, *5*, 8408–8414.

Table of content Graphic and synopsis

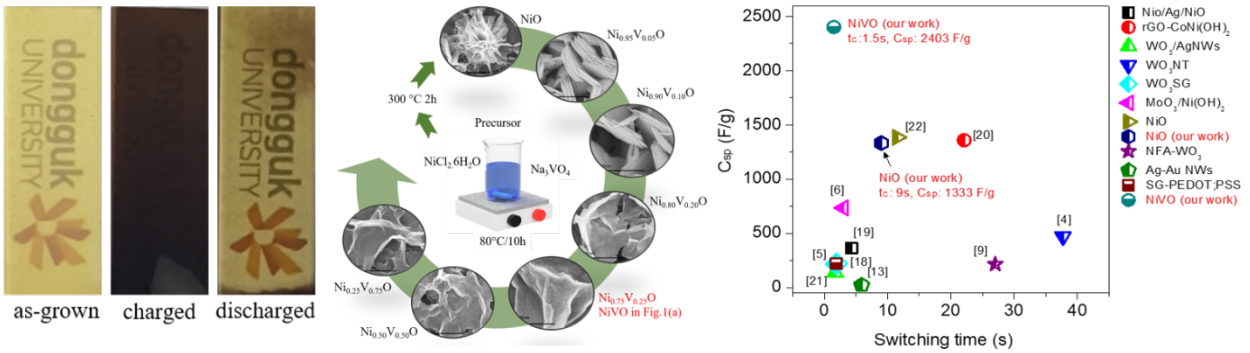

Bimetallic $Ni_{1-x}V_xO$ ($0 \leq x \leq 1$) nanocompounds are fabricated via chemical bath deposition (CBD), tuning the composition ratio (x) systematically to maximize the electrochemical activity. The best optimized bimetallic $Ni_{0.75}V_{0.25}O$ exhibits vastly superior electrochromic and electrochemical energy-storage activities compared to the bare NiO nanosheet electrode.